









Scanning point terahertz source microscopy of unstained comedo ductal carcinoma *in situ*

KOSUKE OKADA,¹ QUENTIN CASSAR,²  HIRONARU MURAKAMI,¹ 
GAËTAN MACGROGAN,³ JEAN-PAUL GUILLET,²  PATRICK
MOUNAIX,²  MASAYOSHI TONOUCI,¹  AND KAZUNORI
SERITA^{1,*} 

¹Institute of Laser Engineering, Osaka University, 2-6 Yamadaoka, Suita, Osaka 565-0871, Japan

²Integration: from Material to Systems Laboratory, UMR CNRS 5218, University of Bordeaux, 33400 Talence, France

³Department of Pathology, Bergonié Institute, 33076 Bordeaux, France

*serita-k@ile.osaka-u.ac.jp

Abstract: Terahertz imaging is an emerging candidate to diagnose breast cancers in a label-free manner. However, detailed terahertz analysis of early stage breast cancers is difficult to achieve owing to its low spatial resolution. In this study, utilizing a probe-less terahertz near-field microscope named scanning point terahertz source microscope, we visualize an unstained comedo ductal-carcinoma-*in-situ* including an architectural structure (comedo necrosis) measuring $\sim\phi 500$ μm , which is known as highly-malignant early-stage breast cancer, in terahertz images for the first time. The outcome is a critical step toward the label-free diagnosis of single early stage cancer lesions with terahertz waves.

© 2022 Optica Publishing Group under the terms of the [Optica Open Access Publishing Agreement](#)

1. Introduction

Terahertz imaging (frequency range: 0.1–30 THz) has provided insights into various applications [1]. Biomedical terahertz spectroscopy and imaging have been developed rapidly in terms of methodology and case studies [2–6]. Among the fields to be investigated intensively, cancer imaging is an important area [7]. Terahertz waves are sensitive to changes in tissue hydration and cellular density associated with cancer emersion [8,9]. Furthermore, it has been reported that different cancer types may exhibit specific absorption peaks related to methylated deoxyribonucleic acid (DNA) [10,11]. Hence, terahertz sensing is expected to be sensitive to the morphological, physiological, and molecular features of malignant tissues in a label-free manner. In particular, it is noteworthy that terahertz imaging is an emerging candidate to identify early stage cancers with higher accuracy than conventional modalities such as magnetic resonance imaging and X-ray computed tomography [7,12].

According to *Global Cancer Statistics 2020* conducted by the American Cancer Society and the International Agency for Research on Cancer, for the first time, female breast cancer is the most typical cancer diagnosed worldwide [13]. Among breast cancer tissues, it is vital to identify early stage cancer “ductal carcinoma *in situ* (DCIS),” which is a proliferation of atypical epithelial cells in the breast ducts, recognized as a precursor of invasive carcinoma [14,15]. Approximately 20% of DCIS cases that have resulted in surgery exhibit an invasive form after the histological examination of the resected tumor [16]. Hence, the problem of “overdiagnosis in DCIS” occurs [17]. To develop an appropriate treatment strategy for patients, it is important not only to detect the presence of DCIS, but also to diagnose the progression risk of the detected DCIS during and after surgery. Although the mechanism of such progression remains unclear [17], DCIS with comedo necrosis, *i.e.*, comedo-DCIS, has a higher proliferation rate and a higher potential to progress to invasive cancer compared with non-comedo lesions [18]. A detailed background of the diagnostic techniques for comedo DCIS is provided in [Supplement 1](#). Therefore, it is

undeniable that the intra- and post-operative discrimination of the comedo-DCIS from other subtypes is crucial.

Many studies indicate that terahertz imaging can aid the visualization of breast tumor tissues, including necrotic ones, in a label-free manner [19–23]. On the other hand, terahertz imaging studies focusing on a single comedo-DCIS lesion have not been conducted because the spatial resolution of typical terahertz systems, dictated by the diffraction limit, is approximately a few millimeters. Such a resolution is insufficient for the analysis of single DCIS lesions typically ranging from 50 to 500 μm . To avoid such problems, we recently developed a probe-less near-field optical microscope with terahertz waves named scanning point terahertz source (SPoTS) microscope [24,25]. The SPoTS microscope operates based on the near-field interaction between the point terahertz-wave source and sample. The point terahertz source is created at the laser-focusing spot near the surface of a nonlinear optical crystal (NLOC) by optical rectification. Therefore, terahertz waves can be confined to an area equivalent to the excitation laser wavelength. Because the sample is set on the surface of the NLOC, this microscope achieves a micrometric spatial resolution ($\sim 10 \mu\text{m}$) and enables the probing of various biological objects, including DCIS, with terahertz waves at the micron scale without any subwavelength probes [4,26–30]. To the best of our knowledge, this is the first time that terahertz waves are successfully used to capture single DCIS lesion [29]. In our previous study, we confirmed that terahertz near-field microscopy can detect the presence of DCIS without requiring labeling. In addition, such a probe-less microscopy technique would contribute significantly to practical applications in cancer diagnosis because probe-based approaches incur several problems, *i.e.*, they require long image-acquisition time and the necessity of large/expensive/rare terahertz emitters/detectors owing to significant terahertz attenuation during measurements, and highly precise alignment [31–35].

In this study, we conducted terahertz near-field imaging and spectroscopy of an unstained single comedo-DCIS lesion on paraffin section in both transmission and reflection modes using the SPoTS microscope. Consequently, for the first time in terahertz cancer imaging, we successfully captured clear terahertz transmission/reflection images of a single comedo-DCIS lesion measuring $\sim \phi 1 \text{ mm}$, as well as successfully distinguished central small comedo necrosis measuring less than $\phi 500 \mu\text{m}$ within the lesion. These results indicate that the SPoTS microscope can identify unstained single comedo-DCIS lesions as well as reveal micrometric architectural structures within a single cancer lesion based on the cell density, owing to its high spatial resolution and high sensitivity without subwavelength probes. The outcome is a critical step toward realizing the terahertz label-free assessment of the “presence” and “malignancy” of early-stage cancers.

2. Experimental setup and sample preparation

2.1. SPoTS microscope

Figures 1(a)–1(b) show a schematic illustration of the SPoTS microscope and an enlarged image of the sample area, respectively. A fiber-coupled femtosecond (fs) pulse laser source (TOPTICA FemtoFiber pro IR: center wavelength of 1.56 μm , maximum power of 350 mW, pulse width of 100 fs, and repetition rate of 80 MHz) was employed as an optical source for the generation and detection of terahertz waves. The laser beam is first separated into pump and probe beams using a beam splitter. The pump pulse is modulated by an optical modulator and irradiates an NLOC, which is a 500- μm -thick (110)-oriented GaAs crystal [36]. As depicted in Fig. 1(b), the pump pulse is focused near the upper surface of the crystal using a focal lens, and a point terahertz source is generated at a laser-focusing spot measuring approximately $\sim \phi 10 \mu\text{m}$ via optical rectification [37]. The inspected sample is placed in the near-field domain of the point terahertz source, *i.e.*, on the upper surface of the GaAs crystal. The localized-intense-terahertz pulse beam emitted from the point source is transmitted through the sample or reflected at the

interface between the sample and GaAs. Hence, terahertz measurement with a high spatial resolution similar to the pump laser wavelength can be realized without using subwavelength probes. To enhance the spatial resolution, we must consider the terahertz beam divergence $W(z)$

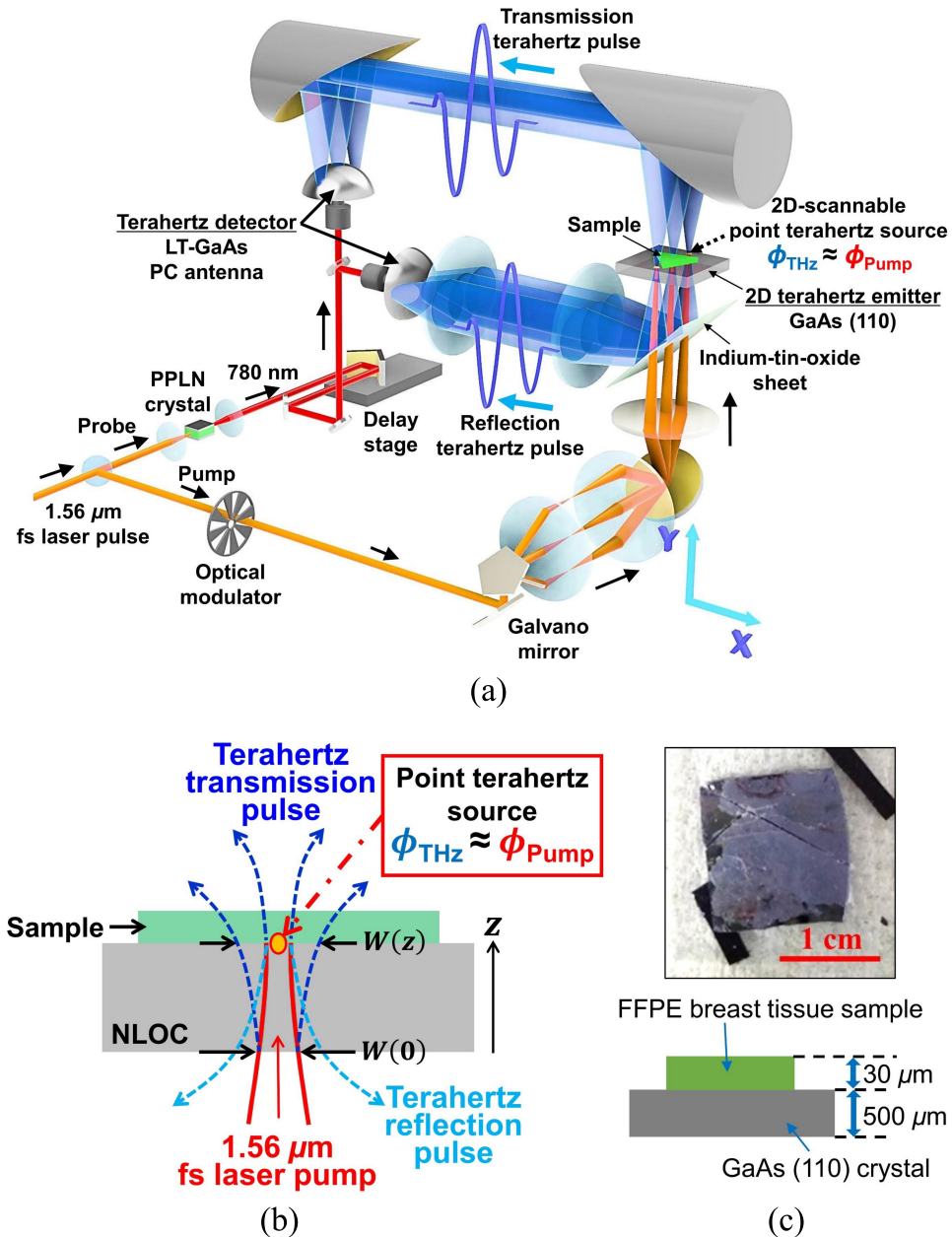


Fig. 1. Schematic illustration of scanning point terahertz source microscope: (a) overall view and (b) around sample. (c) Photograph of formalin-fixed paraffin-embedded (FFPE) breast tissue sample deposited on GaAs (110) crystal (upper), and its cross-sectional view (lower).

in the NLOC, which can be expressed as

$$W(z) = W(0) \sqrt{1 + \left(\frac{z \cdot \lambda_{\text{THz}}}{\pi \cdot W(0)} \right)^2}, \quad (1)$$

where z and λ_{THz} are the distance from the bottom face of the NLOC and the center wavelength of the incident terahertz beam, respectively; $W(0)$ is the initial terahertz beam diameter [24]. As shown in this equation, the terahertz divergence is proportional to the NLOC thickness. In fact, we experimentally confirmed that the spatial resolution increased as the NLOC thickness decreased [25]. Therefore, to obtain a higher spatial resolution, a thinner NLOC should be prepared and the pump laser beam should be focused at the output surface of the crystal using a high-numerical-aperture lens. Finally, the terahertz waves were detected by a spiral-shaped low-temperature-grown (LT-) GaAs photoconductive (PC) antenna detector driven by a wavelength-converted probe pulse beam (780 nm) via a periodically poled LiNbO₃ (PPLN) crystal. We were able to obtain terahertz transmission and reflection time-domain waveforms with broad frequency ranges up to approximately 4 THz and 2.5 THz by monitoring the amplitude of the terahertz pulses while moving a delay stage. The characteristics of the terahertz transmission and reflection time-domain waveforms measured at the GaAs-bare region (*i.e.*, no sample) are provided in Section 2 of [Supplement 1](#). Terahertz imaging in transmission and reflection modes was performed via the high-speed two-dimensional (2D) scanning of the point terahertz source over the GaAs crystal in the X - Y direction using a galvano mirror. The current spatial resolution for the terahertz imaging was $\sim 10 \mu\text{m}$ [30]. In this study, the image acquisition speed was set to 90 s/image for 128×128 pixels to maintain a good signal-to-noise ratio. The field of view (FOV) of the microscope was approximately $280 \mu\text{m} \times 280 \mu\text{m}$. The acquisition of the terahertz image of a region larger than the FOV was achieved by the combination of several terahertz images within the size of the FOV. The details of the FOV of the SPoTS microscope are described in Section 3 of [Supplement 1](#).

2.2. Formalin-fixed paraffin-embedded (FFPE) human breast cancer tissue sample

Because the measurements by the SPoTS microscope are based on a near-field interaction between a sample and a point terahertz source, the tissue sample must be placed in contact with the GaAs terahertz-generation crystal. In this study, we inspected FFPE human breast cancer tissues that were directly deposited on GaAs crystal. Figure 1(c) shows a photograph of a 30- μm -thick FFPE breast tissue section deposited on a 500- μm -thick GaAs crystal (upper) and its cross-sectional view (lower). Formalin-fixation and paraffin-embedding techniques are used to preserve biological tissues without alteration [38]. The breast tissue sample was excised from a 44-year-old woman and included DCIS (containing comedo-type), invasive ductal carcinoma, and other normal tissues such as normal ducts and lobules, as well as adipose and collagen fibrosis tissues. Lipids were purged from adipose tissue during paraffin embedding. The distribution areas of these tissues were identified by a pathologist using hematoxylin-eosin-saffron (HES)-stain.

3. Results and discussion

Figures 2(a)–2(b) show the optical- and HES-stained- images of comedo-type DCIS. In the HES-stained image shown in Fig. 2(b), the pink-stained regions represent the cell cytoplasm. The purple-stained areas represent the presence of nucleic acids/nuclei, orange/yellow stained regions correspond to collagen fibers, and white regions correspond to adipose tissue or retraction artifact. Comedo DCIS is characterized by ductal structures involved by a rim of carcinoma cells visible at the periphery of the duct (peripheral neoplasm) and central tumoral necrosis (comedo necrosis). It is noteworthy that terahertz imaging was performed on an unstained sample on the paraffin section shown in Fig. 2(a).

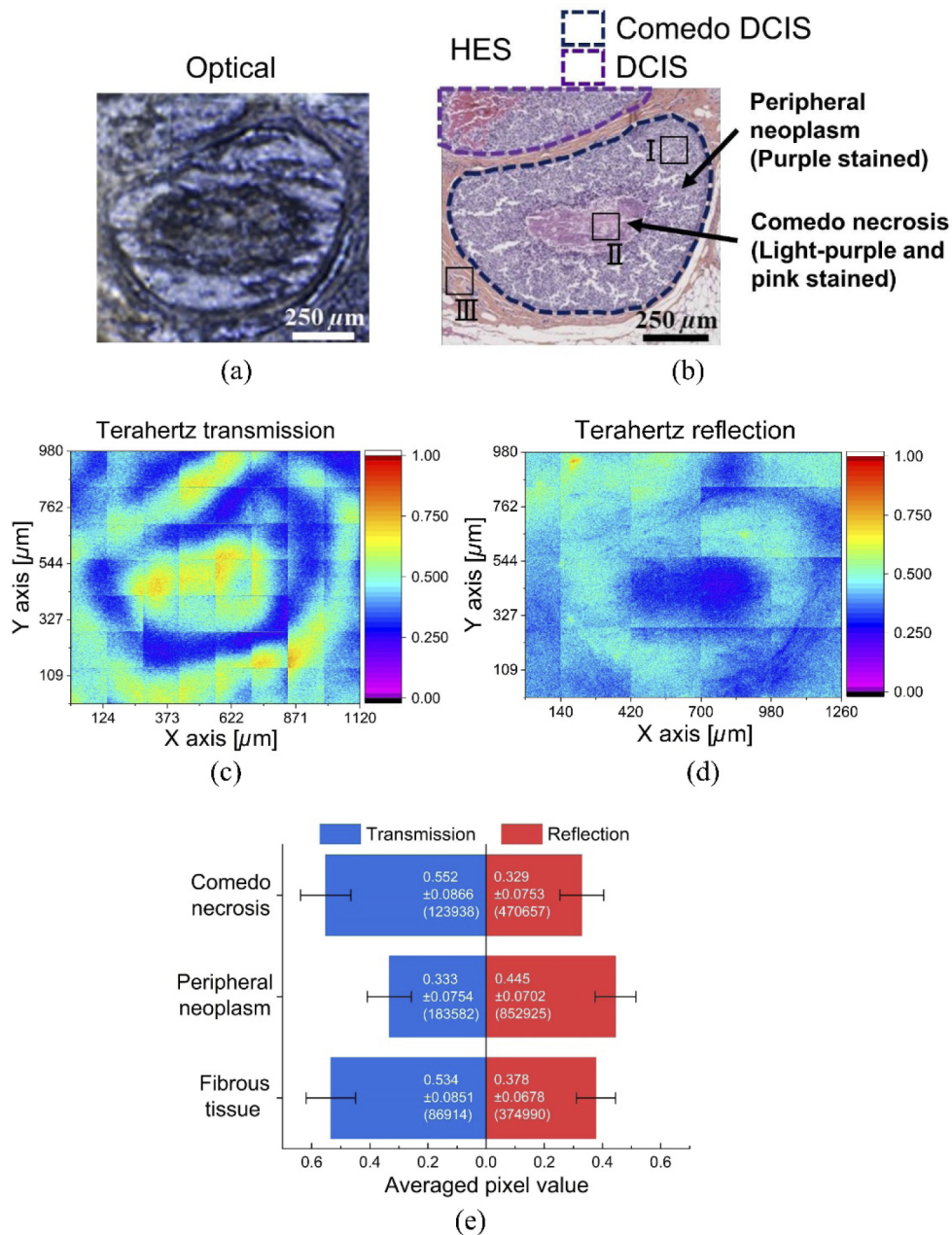


Fig. 2. (a) Optical-, (b) hematoxylin-eosin-saffron (HES)-stained-, (c) terahertz-transmission-, and (d) terahertz-reflection- images of comedo-type ductal carcinoma *in situ* (DCIS). Terahertz images were obtained at highest positive peaks of time-domain terahertz waveforms. In the HES image, DCIS and comedo DCIS compartments are highlighted by dotted purple and dark-blue lines. Fibrous region corresponds to orange/yellow-stained areas around comedo DCIS. (e) Averaged pixel value (APV) of each tissue in transmission- and reflection-terahertz image shown in Figs. 2(c)–2(d). The selected regions of interest in the images for the APV calculations for the three regions are displayed in Section 4 of Supplement 1. Error bars indicate standard deviations (SDs). The numbers in the bars indicate the APVs, SDs, and the total number of pixels used in the calculation of APVs (in parentheses).

Figures 2(c)–2(d) show the terahertz-transmission- and terahertz-reflection- images of the comedo-type DCIS. These images were obtained at highest positive peaks of terahertz time-domain waveforms. Because the lesion size is larger than the FOV of the SPoTS microscope, these terahertz images were made by the combination of several terahertz images. In both the terahertz images, it was discovered that the single comedo DCIS lesion measuring $\sim\phi 1$ mm in the center position was clearly distinguished from periductal fibrous tissue. Furthermore, within the DCIS lesion, the comedo necrosis measuring $\sim\phi 500$ μm was similarly clearly distinguished from the peripheral neoplasm region. These terahertz images correlated well with the corresponding HES-stained images shown in Fig. 2(b). It is noteworthy that the single comedo DCIS and the micrometric architectural structure within its lesion (comedo necrosis) were successfully imaged with a probe-less and fiber-laser-based terahertz system for the first time, owing to the high spatial resolution of the SPoTS microscopy.

To statistically elucidate such differences, we present the averaged pixel values (APVs) of the three different regions in the terahertz images, as shown in Fig. 2(e). The selected regions of interest (ROI) in the images for the APV calculations for the three regions are described in Section 4 of Supplement 1. The error bars indicate the standard deviations (SDs). The numbers in the bars indicate the APVs, SDs, and the total number of the pixels of the ROIs used for the APV calculations (in parentheses). As shown in both datasets, the APVs differed in the following order: [Transmission] comedo necrosis > fibrous tissue > peripheral neoplasm, [Reflection] peripheral neoplasm > fibrous tissue > comedo necrosis. Examining the APVs in addition to their SDs for different tissues in more detail, the transmission and reflection APVs of the peripheral neoplasm were 0.201 lower and 0.067 higher than those of the periductal fibrous (benign) tissue, respectively. Meanwhile, the transmission and reflection APVs of the comedo necrosis were 0.219 higher and 0.116 lower than those of the peripheral neoplasm, respectively. Furthermore, we discovered that the APVs between the comedo necrosis and fibrous tissue slightly differed. Specifically, the terahertz transmission and reflection APVs in the comedo necrosis area were 0.018 higher and 0.049 lower compared with those in the fibrous tissue area, respectively. It is noted that the SD values of the tissue APVs were high with respect to the abovementioned differences between the APVs. Additional studies on a larger set of samples are required to validate the relevance of these APV differences.

To compare the terahertz signals (the pixel values) of the comedo necrosis, peripheral neoplasm, and fibrous tissue in the images in more detail, we measured the terahertz transmission and reflection time-domain waveforms at several points in the three tissues, as presented in Figs. 3(a)–3(b). As shown in the enlarged views around the main peaks, the electric field intensities at the highest peak points in the waveforms at approximately 4 ps (E), which correspond to the imaging points, differed among the tissues: [Transmission] $E_{\text{Necrosis}} (2.63) > E_{\text{Fibrous}} (2.59) > E_{\text{Neoplasm}} (2.22)$, [Reflection] $E_{\text{Neoplasm}} (0.792) > E_{\text{Fibrous}} (0.737) > E_{\text{Necrosis}} (0.662)$. The results are consistent with the abovementioned tendency of the APVs of the terahertz images. This tendency also shows the consistency of the experimental results obtained in both the transmission and reflection modes, thereby confirming that the SPoTS microscope accurately detected minute lesions. Regarding spectroscopic analysis, Figs. 3(c)–3(d) show the terahertz transmission and reflection frequency spectra of each tissue calculated from the terahertz time-domain waveforms shown in Figs. 3(a)–3(b), respectively. These spectra were normalized by the spectrum of the fibrous tissue. It was discovered that the spectra of the terahertz electric fields were broadly separated and the differences were evident, particularly in the frequency range above 0.5 THz. Particularly regarding the spectra of the comedo necrosis and peripheral neoplasm, the transmission terahertz electric fields were higher, where the reflection ones were lower in the comedo necrosis. Note that the absorption peaks (ex. 1.7, 1.9, 2.2, 2.4 THz) were due to water vapor [39], and no specific absorption peaks related to the tissues could be observed.

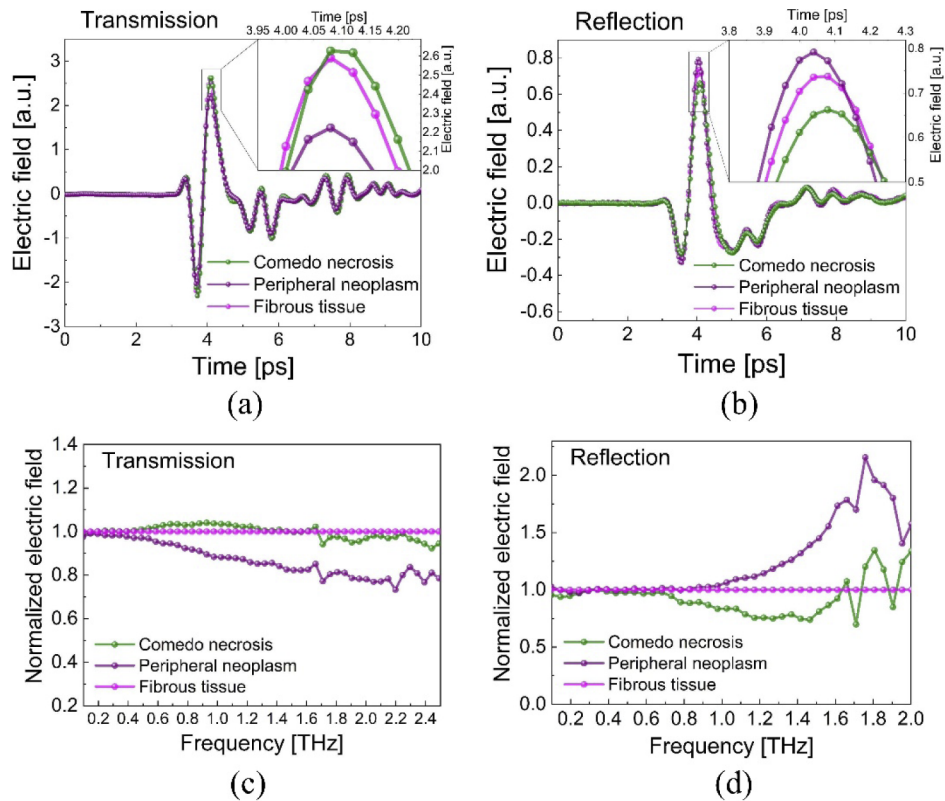


Fig. 3. (a) Transmission- and (b) reflection- terahertz time-domain waveforms of comedo necrosis, peripheral neoplasm, and fibrous tissue. (c) Transmission- and (d) reflection-frequency spectra of them normalized by the spectrum of the fibrous tissue. To extract the data, we obtained terahertz waveforms measured at several different locations of comedo necrosis (three points), peripheral neoplasm (three points), and fibrous tissue (three points). The displayed waveforms are their averaged plots.

The results above suggest that terahertz attenuation increased in the following order: peripheral neoplasm > fibrous tissue > comedo necrosis. This phenomenon is attributable to the difference in epithelial cell density. In our previous study [29,30], terahertz-attenuation differences were observed between DCIS and IDC lesions, which was attributed to micrometric differences in the cell density. Herein, we discuss the results obtained in this study based on the cell density, as in our previous studies [29,30]. Figures 4(a)–4(c) show the cellular-level HES images of the peripheral neoplasm, comedo necrosis, and periductal fibrous tissue highlighted by black boxes in Fig. 2(b), respectively. As shown, the epithelial cell nuclei, which were stained in purple, were abundant at the periphery of the duct involved by comedo DCIS (peripheral neoplasm) compared with those at the comedo necrosis and the fibrous tissue surrounding the duct. No visible nuclei were present in the comedo necrosis because the tumor cells had undergone necrosis owing to insufficient vascularization. Because the cell nucleus contains many nucleic acids in a small area and is therefore denser than other cellular components, it was assumed that the increase in the nuclear density enhanced terahertz absorption and/or scattering [29,30]. Hence, terahertz attenuation in the comedo necrosis and the fibrous tissue was lower than that in the peripheral neoplasm. In fact, Oh *et al.* reported that the necrotic region in paraffin-embedded brain cancer presented low terahertz reflections compared with the adjacent neoplasm region because the

necrotic area had a lower cell density than the neoplasm area [40]. Therefore, the epithelial cell density significantly affected the terahertz image contrast between the neoplasm and other regions. Regarding the comedo necrosis and fibrous tissue, our results indicated a slightly lower terahertz attenuation in the comedo necrotic region. However, considering the standard deviation displayed in Fig. 2(e), the difference is too small to discuss it as a significant result. Additional studies are required to validate the difference. Furthermore, it is noteworthy that paraffin-embedding techniques dehydrate the samples and purge lipid components. Therefore, water and lipids should not significantly affect the image contrast of FFPE samples.

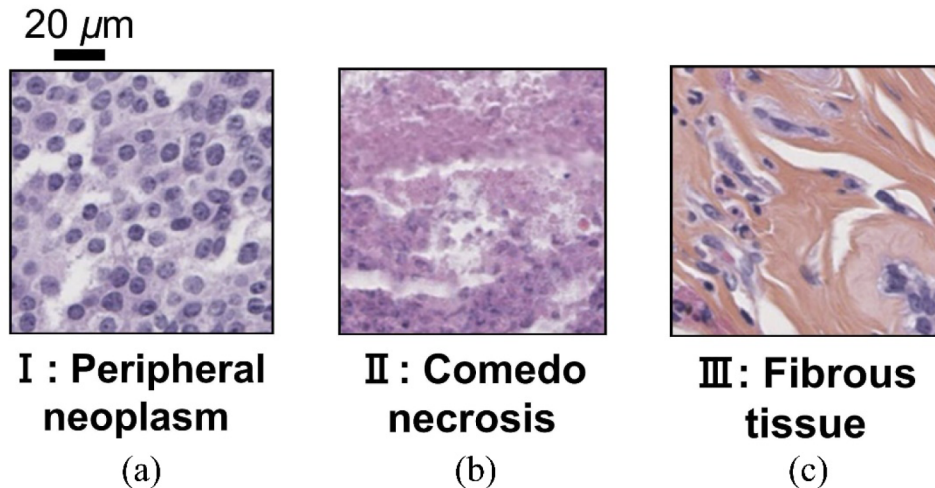


Fig. 4. Hematoxylin-eosin-saffron (HES)-stained images of (a) region I (peripheral neoplasm), (b) region II (comedo necrosis), and (c) region III (fibrous tissue) at cellular level, as labeled in Fig. 2(b).

4. Conclusion

To investigate the capability of probe-less terahertz microscopy for the analysis of comedo-DCIS known as highly-malignant early-stage human breast cancer, we performed terahertz near-field transmission/reflection spectroscopy and the imaging of the lesion on paraffin section using an SPoTS microscope. Consequently, for the first time, we successfully visualized an unstained single comedo-DCIS lesion ($\sim\phi 1$ mm) in both transmission- and reflection-terahertz images, while identifying a small architectural structure within the lesion, *i.e.*, the comedo necrosis ($\sim\phi 500$ μm). The comedo necrotic region indicated a lower terahertz attenuation than the peripheral neoplasm region, based on the difference in the epithelial cell density. These results indicated the potential of terahertz imaging for the detection of unstained comedo DCIS, which is an important factor in DCIS diagnosis. In addition, the SPoTS microscope can analyze micrometric architectural structures within a single small cancer lesion based on cell density, owing to its high spatial resolution and high sensitivity without requiring subwavelength probes. These findings may be a critical step toward realizing the terahertz label-free diagnosis of DCIS and other early stage cancers.

For intraoperative diagnostic applications, fresh tissues must be measured. On-site terahertz measurements of hydrated tissues can be conducted in reflection mode because the large absorption of terahertz waves by water molecules renders it difficult to implement high signal-to-noise-ratio measurements in transmission mode. Because the hydration level differs for tumor and benign tissues [41], an enhanced terahertz contrast between these tissues compared with that in the

present study should be realized in future studies [40]. Additionally, iced or quickly dried tissues would be diagnosed in both transmission and reflection modes. For post-operative examination, because the tissue sample involved is desiccated, terahertz analysis can be performed in both modes. Further improvements pertaining to the spatial resolution of the SPoTS microscope to a submicron level may enable us to visualize other DCIS architectural subtypes (cribriform and micropapillary types) [14] and each nucleus of breast cancer cells, which are important for more precise DCIS diagnosis. Information regarding DNA methylation, which may be associated with prognostic features in DCIS [42], may be extracted via sensitivity-enhanced terahertz spectroscopic sensing at approximately 1.6 THz [10]. For clinical applications, portable SPoTS inspection devices should be developed by introducing fiber optics and system miniaturization. Hence, terahertz microscopic sensing using a probe-less SPoTS microscope can potentially provide micrometric, quantitative, and objective information that facilitate early stage cancer detection and grading in a label-free manner during and after surgery. Furthermore, implementing the SPoTS microscope along with other laser-pumped microscopy systems (nonlinear microscopy, photoacoustic microscopy, optical coherence tomography [43], etc.) may be beneficial because each of the optical modalities offers inherent advantages and disadvantages for breast cancer diagnosis [44]. Although the abovementioned approach may not yet be ideal for on-site diagnoses, the use of an advanced image processing/database pertaining to HES-stained tissues aided by artificial intelligence [23,45] would compensate for its challenges and provide more reliable information regarding the lesions.

Funding. Japan Society for the Promotion of Science (JP18H01499, JP20H00247, JP20K20536); Fusion Oriented REsearch for disruptive Science and Technology (JPMJFR2029); New Aquitania Region.

Acknowledgments. Portions of this work were presented at JSAP-OSA joint symposium in 2021, 12a-N405-6.

Ethical statement. Human tissue analysis and measurements were performed in view of the fundamental ethical principles stipulated in the Declaration of Helsinki and its subsequent revisions. Samples were used in accordance with the ethical regulations of the Bergonié Institute Tissue Bank. Written informed consent from each patient undergoing breast surgery was collected, stipulating their agreement regarding the use of their tissues for research purposes.

Disclosures. The authors declare no conflicts of interest.

Data availability. Data underlying the results presented in this paper are not publicly available at this time but may be obtained from the authors upon reasonable request.

Supplemental document. See Sections 1-4 of [Supplement 1](#) for supporting content.

References

1. D. M. Mittleman, "Twenty years of terahertz imaging," *Opt. Express* **26**(8), 9417–9431 (2018).
2. J. H. Son, *Terahertz Biomedical Science and Technology* (CRC press, US, 2014).
3. T. L. Cocker, D. Peller, P. Yu, J. Repp, and R. Huber, "Tracking the ultrafast motion of a single molecule by femtosecond orbital imaging," *Nature* **539**(7628), 263–267 (2016).
4. K. Serita, E. Matsuda, K. Okada, H. Murakami, I. Kawayama, and M. Tonouchi, "Invited Article: Terahertz microfluidic chips sensitivity-enhanced with a few arrays of meta-atoms," *APL Photonics* **3**(5), 051603 (2018).
5. Y. Deng, J. A. McKinney, D. K. George, K. A. Niessen, A. Sharma, and A. G. Markelz, "Near-Field Stationary Sample Terahertz Spectroscopic Polarimetry for Biomolecular Structural Dynamics Determination," *ACS Photonics* **8**(2), 658–668 (2021).
6. K. Liu, R. Zhang, Y. Liu, X. Chen, K. Li, and E. Pickwell-Macpherson, "Gold nanoparticle enhanced detection of EGFR with a terahertz metamaterial biosensor," *Biomed. Opt. Express* **12**(3), 1559–1567 (2021).
7. J. H. Son, S. J. Oh, and H. Cheon, "Potential clinical applications of terahertz radiation," *J. Appl. Phys.* **125**(19), 190901 (2019).
8. E. Pickwell, A. J. Fitzgerald, B. E. Cole, P. F. Taday, R. J. Pye, T. Ha, M. Pepper, and V. P. Wallace, "Simulating the response of terahertz radiation to basal cell carcinoma using ex vivo spectroscopy measurements," *J. Biomed. Opt.* **10**(6), 064021 (2005).
9. S. Sy, S. Huang, Y. X. Wang, J. Yu, A. T. Ahuja, Y. T. Zhang, and E. Pickwell-MacPherson, "Terahertz spectroscopy of liver cirrhosis: investigating the origin of contrast," *Phys. Med. Biol.* **55**(24), 7587–7596 (2010).
10. H. Cheon, H. J. Yang, S. H. Lee, Y. A. Kim, and J. H. Son, "Terahertz molecular resonance of cancer DNA," *Sci. Rep.* **6**(1), 37103 (2016).
11. H. Cheon, H.-J. Yang, M. Choi, and J.-H. Son, "Effective demethylation of melanoma cells using terahertz radiation," *Biomed. Opt. Express* **10**(10), 4931–4941 (2019).

12. K. I. Zaytsev, K. G. Kudrin, V. E. Karasik, I. V. Reshetov, and S. O. Yurchenko, "In vivo terahertz spectroscopy of pigmentary skin nevi: Pilot study of non-invasive early diagnosis of dysplasia," *Appl. Phys. Lett.* **106**(5), 053702 (2015).
13. H. Sung, J. Ferlay, R. L. Siegel, M. Laversanne, I. Soerjomataram, A. Jemal, and F. Bray, "Global cancer statistics 2020: GLOBOCAN estimates of incidence and mortality worldwide for 36 cancers in 185 countries," *CA A Cancer J Clin* **71**(3), 209–249 (2021).
14. K. L. Gorringer and S. B. Fox, "Ductal carcinoma *in situ* biology, biomarkers, and diagnosis," *Front. Oncol.* **7**, 248 (2017).
15. D. C. Allred, "Ductal carcinoma in situ: terminology, classification, and natural history," *JNCI Monographs* **2010**(41), 134–138 (2010).
16. "Treatment of ductal carcinoma in situ: an uncertain harm-benefit balance," *Prescrire Int.* **22**(144), 298–303 (2013).
17. M. van Seijen, E. H. Lips, A. M. Thompson, S. Nik-Zainal, A. Futreal, E. S. Hwang, E. Verschuur, J. Lane, J. Jonkers, D. W. Rea, J. Wesseling, and J. Wesseling, "Ductal carcinoma in situ: to treat or not to treat, that is the question," *Br. J. Cancer* **121**(4), 285–292 (2019).
18. M. P. Shekhar, L. Tait, R. J. Pauley, G. S. Wu, S. J. Santner, P. Nangia-Makker, V. Shekhar, H. Nassar, D. W. Visscher, G. H. Heppner, and F. R. Miller, "Comedo-ductal carcinoma in situ: A paradoxical role for programmed cell death," *Cancer Biol. Ther.* **7**(11), 1774–1782 (2008).
19. A. J. Fitzgerald, V. P. Wallace, M. Jimenez-Linan, L. Bobrow, R. J. Pye, A. D. Purushotham, and D. D. Arnone, "Terahertz pulsed imaging of human breast tumors," *Radiology* **239**(2), 533–540 (2006).
20. Q. Cassar, A. Al-Ibadi, L. Mavarani, P. Hillger, J. Grzyb, G. MacGrogan, T. Zimmer, U. R. Pfeiffer, J. P. Guillet, and P. Mounaix, "Pilot study of freshly excised breast tissue response in the 300–600 GHz range," *Biomed. Opt. Express* **9**(7), 2930–2942 (2018).
21. P. C. Ashworth, E. Pickwell-MacPherson, E. Provenzano, S. E. Pinder, A. D. Purushotham, M. Pepper, and V. P. Wallace, "Terahertz pulsed spectroscopy of freshly excised human breast cancer," *Opt. Express* **17**(15), 12444–12454 (2009).
22. T. Bowman, M. El-Shenawee, and L. K. Campbell, "Terahertz transmission vs reflection imaging and model-based characterization for excised breast carcinomas," *Biomed. Opt. Express* **7**(9), 3756–3783 (2016).
23. Q. Cassar, S. Caravera, G. MacGrogan, T. Bücher, P. Hillger, U. Pfeiffer, T. Zimmer, J. P. Guillet, and P. Mounaix, "Terahertz refractive index-based morphological dilation for breast carcinoma delineation," *Sci. Rep.* **11**(1), 6457 (2021).
24. K. Serita, S. Mizuno, H. Murakami, I. Kawayama, Y. Takahashi, M. Yoshimura, Y. Mori, J. Darmo, and M. Tonouchi, "Scanning laser terahertz near-field imaging system," *Opt. Express* **20**(12), 12959–12965 (2012).
25. K. Okada, K. Serita, Z. Zang, H. Murakami, I. Kawayama, Q. Cassar, G. MacGrogan, J. P. Guillet, P. Mounaix, and M. Tonouchi, "Scanning laser terahertz near-field reflection imaging system," *Appl. Phys. Express* **12**(12), 122005 (2019).
26. K. Serita, H. Murakami, I. Kawayama, Y. Takahashi, M. Yoshimura, Y. Mori, and M. Tonouchi, "Evaluation of human hairs with terahertz wave," *Opt. Eng.* **53**(3), 031205 (2014).
27. H. Murakami, K. Serita, Y. Maekawa, S. Fujiwara, E. Matsuda, S. Kim, I. Kawayama, and M. Tonouchi, "Scanning laser THz imaging system," *J. Phys. D: Appl. Phys.* **47**(37), 374007 (2014).
28. K. Serita, H. Murakami, I. Kawayama, and M. Tonouchi, "A terahertz-microfluidic chip with a few arrays of asymmetric meta-atoms for the ultra-trace sensing of solutions," *Photonics* **6**(1), 12 (2019).
29. K. Okada, K. Serita, Q. Cassar, H. Murakami, G. MacGrogan, J. P. Guillet, P. Mounaix, and M. Tonouchi, "Terahertz near-field microscopy of ductal carcinoma *in situ* (DCIS) of the breast," *J. Phys. Photonics* **2**(4), 044008 (2020).
30. K. Okada, Q. Cassar, H. Murakami, G. MacGrogan, J. P. Guillet, P. Mounaix, M. Tonouchi, and K. Serita, "Label-Free Observation of Micrometric Inhomogeneity of Human Breast Cancer Cell Density Using Terahertz Near-Field Microscopy," *Photonics* **8**(5), 151 (2021).
31. U. Schade, K. Holldack, P. Kuske, G. Wüstefeld, and H.-W. Hübers, "THz near-field imaging employing synchrotron radiation," *Appl. Phys. Lett.* **84**(8), 1422–1424 (2004).
32. C.-M. Chiu, H.-W. Chen, Y.-R. Huang, Y.-J. Hwang, W.-J. Lee, H.-Y. Huang, and C.-K. Sun, "All-terahertz fiber-scanning near-field microscopy," *Opt. Lett.* **34**(7), 1084–1086 (2009).
33. Z. Li, S. Yan, Z. Zang, G. Geng, Z. Yang, J. Li, L. Wang, C. Yao, H. L. Cui, C. Chan, and H. Wang, "Single cell imaging with near-field terahertz scanning microscopy," *Cell Prolif.* **53**(4), e12788 (2020).
34. Z. Yang, D. Tang, J. Hu, M. Tang, M. Zhang, H. L. Cui, L. Wang, C. Chang, C. Fan, and J. Li, "Near-Field Nanoscopic Terahertz Imaging of Single Proteins," *Small* **17**(3), 2005814 (2021).
35. O. Smolyanskaya, N. Chernomyrdin, A. Konovko, K. Zaytsev, I. Ozheredov, O. Cherkasova, M. Nazarov, J.-P. Guillet, S. Kozlov, Y. Kistenev, J.-L. Coutaz, P. Mounaix, V. Vaks, J.-H. Son, H. Cheon, V. Wallace, Y. Feldman, I. Popov, A. Yaroslavsky, A. Shkurinov, and V. Tuchin, "Terahertz biophotonics as a tool for studies of dielectric and spectral properties of biological tissues and liquids," *Prog. Quantum Electron.* **62**, 1–77 (2018).
36. M. Nagai, K. Tanaka, H. Ohtake, T. Bessho, T. Sugiura, T. Hirosumi, and M. Yoshida, "Generation and detection of terahertz radiation by electro-optical process in GaAs using 1.56 μm fiber laser pulses," *Appl. Phys. Lett.* **85**(18), 3974–3976 (2004).

37. C. Fumeaux, H. Lin, K. Serita, W. Withayachumnankul, T. Kaufmann, M. Tonouchi, and D. Abbott, "Distributed source model for the full-wave electromagnetic simulation of nonlinear terahertz generation," *Opt. Express* **20**(16), 18397–18414 (2012).
38. M. Doleshal, A. A. Magotra, B. Choudhury, B. D. Cannon, E. Labourier, and A. E. Szafranska, "Evaluation and validation of total RNA extraction methods for microRNA expression analyses in formalin-fixed, paraffin-embedded tissues," *The Journal of Molecular Diagnostics* **10**(3), 203–211 (2008).
39. X. Xin, H. Altan, A. Saint, D. Matten, and R. R. Alfano, "Terahertz absorption spectrum of para and ortho water vapors at different humidities at room temperature," *J. Appl. Phys.* **100**(9), 094905 (2006).
40. S. J. Oh, S.-H. Kim, Y. B. Ji, K. Jeong, Y. Park, J. Yang, D. W. Park, S. K. Noh, S.-G. Kang, Y.-M. Huh, J.-H. Son, and J.-S. Suh, "Study of freshly excised brain tissues using terahertz imaging," *Biomed. Opt. Express* **5**(8), 2837–2842 (2014).
41. G. I. McIntyre, "Cell hydration as the primary factor in carcinogenesis: A unifying concept," *Med. Hypotheses* **66**(3), 518–526 (2006).
42. J. M. Pang, S. Deb, E. A. Takano, D. J. Byrne, N. Jene, A. Boulghourjian, A. Holliday, E. Millar, C. S. Lee, S. A. O'Toole, A. Dobrovic, and S. B. Fox, "Methylation profiling of ductal carcinoma *in situ* and its relationship to histopathological features," *Breast Cancer Res.* **16**(5), 423 (2014).
43. A. J. Fitzgerald, X. Tie, M. J. Hackmann, B. Cense, A. P. Gibson, and V. P. Wallace, "Co-registered combined OCT and THz imaging to extract depth and refractive index of a tissue-equivalent test object," *Biomed. Opt. Express* **11**(3), 1417–1431 (2020).
44. G. Balasundaram, C. Krafft, R. Zhang, K. Dev, R. Bi, M. Moothanchery, J. Popp, and M. Olivo, "Biophotonic technologies for assessment of breast tumor surgical margins—A review," *J. Biophotonics* **14**(1), e202000280 (2021).
45. W. Liu, R. Zhang, Y. Ling, H. Tang, R. She, G. Wei, X. Gong, and Y. Lu, "Automatic recognition of breast invasive ductal carcinoma based on terahertz spectroscopy with wavelet packet transform and machine learning," *Biomed. Opt. Express* **11**(2), 971–981 (2020).